Capillarity

Vol. 14, No. 3, p. 63-71, 2025

Original article

A more rigorous mathematical model for capillary imbibition of CO_2 in shale gas formations

Jun Zhang[1], Boyun Guo[2]*, Vincent Nana Boah Amponsah[2]

[1]*College of Oil and Gas Engineering, Northeast Petroleum University, Daqing 163318, P. R. China*
[2]*College of Engineering, University of Louisiana at Lafayette, Lafayette LA 70504, USA*

Keywords:
Capillary pressure
imbibition
mathematical model
shale gas
CO_2

Cited as:
Zhang, J., Guo, B., Amponsah, V. N. B. A more rigorous mathematical model for capillary imbibition of CO_2 in shale gas formations. Capillarity, 2025, 14(3): 63-71.
https://doi.org/10.46690/capi.2025.03.01

Abstract:
A mathematical model was derived in this study to reveal the mechanism of CO_2 imbibition in shale formations considering the combined effects of capillary force and viscous force in concave curved triangle pore channels surrounded by different solid materials with different wettability. The model reveals that CO_2 imbibition depth is proportional to the square root of CO_2 soaking time, square root of the pore size determined by grain size, square root of interfacial tension and cosine of contact angle, and inversely proportional to the square root of CO_2 viscosity. Up to three solid wall materials with different contact angles can be considered in the model. Using the average contact angle for the three materials overestimates the imbibition distance. CO_2 imbibition is faster in concave curved triangle pores than in equivalent circular-shaped pores. The dimensionless geometry correction factor is less than unity ($\alpha = 0.81$). The newly developed imbibition model can be used for predicting the maximum time of imbibition between parallel fractures in multi-fractured shale formations.

1. Introduction

The advantages and limitations of using CO_2 as hydraulic fracturing fluid were reported based on operations over 450 wells in conventional gas/oil reservoirs back 40 years ago (Sinal and Lancaster, 1987). Experimental studies were conducted on the growth behavior of CO_2-induced fractures in a layered tight sandstone formation (Zou et al., 2018). CO_2 fracturing was found to increase oil productivity in tight oil reservoirs by 4- to 20-fold (Song et al., 2019). Shale oil formations are less water-wet than sandstone formations due to their organics (kerogen) contents in rock matrix. CO_2 has higher affinity to the organics and has been found to be more effective than water for fracturing shale oil wells to increase productivity. CO_2 was considered commercially viable for shale gas and oil production due to its ability to simultaneously reduce CO_2 emissions to the atmosphere through sequestration while enhancing gas extraction from shale gas reservoirs (Middleton et al., 2014). Fakher and Heidari (2021) analyzed the main factors impacting on the applicability of CO_2-hydraulic fracturing, including the properties of CO_2, reservoir rock and fluid, and fracturing proppants. Yang et al. (2022) presented a fundamental study on CO_2-fracturing in development of unconventional oil and gas reservoirs.

Recently Gupta and Verma (2023) provided a review of studies on CO_2 geo-storage and utilization for hydraulic-fracturing shale gas/oil reservoirs. They concluded that developing a thorough understanding of the interactions between CO_2 and shale rock is quite challenging. This is partially due to lack of research and limited knowledge in the field. This promoted more research work in the area of CO_2 fracturing

Yandy Scientific Press

*Corresponding author.
E-mail address: Zhangjun410410@nepu.edu.cn (J, Zhang); boyun.guo@louisiana.edu (B, Guo); vincent.amponsah1@louisiana.edu (V. N. B, Amponsah).

Received January 29, 2025; revised February 20, 2025; accepted March 10, 2025; available online March 13, 2025.

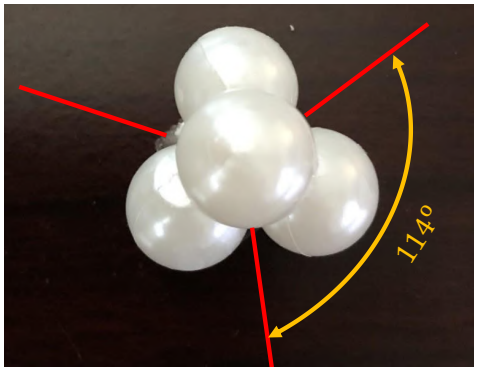

Fig. 1. The base unit of an ideal pack of spheric grains of uniform sizes.

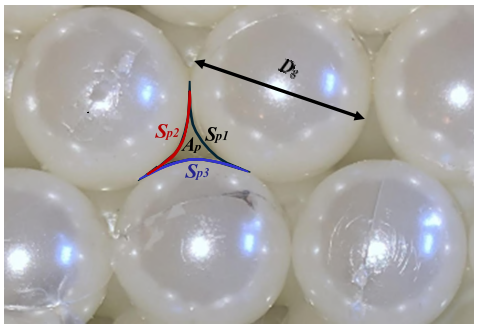

Fig. 2. A concave curved triangle model for the pore space between three spheric grains of different wetting properties.

and the interaction of CO_2 with shale rocks. Most researchers believe that spontaneous imbibition dominated by capillary force is responsible for CO_2 retention in shale gas/oil formations (Cai et al., 2023). It is challenging to model the spontaneous imbibition due to the complex imbibition mechanisms involving multi-influencing factors such as petrophysical properties of shales and fluid properties. Cai and Yu (2011) presented a discussion of the effect of path tortuosity on the capillary imbibition in porous media. Cai et al. (2014) published a generalized model for spontaneous imbibition based on Hagen-Poiseuille flow in tortuous capillaries with variably shaped apertures, not including concave curved triangle pore channels. However, most previous studies assume circular shape of cross-sections of capillaries and uniform contact angle throughout the capillaries.

This study presents a spontaneous-viscous imbibition model for CO_2-soaking in shale plays with mixed wettability and non-circular capillaries. The model considers the combined effects of capillary force and viscous force in concave curved triangle pore channels surrounded by three types of solid materials with different contact angles. Sensitivity analyses are presented and major factors affecting CO_2 soaking in shale oil reservoirs are identified.

2. Mathematical model

Mass transfer in nanoscale pore channels is driven by capillary force, resisted by viscous friction force, and promoted or demoted by gravitational force, depending on orientation of the flow relative to gravity. For the fluid imbibition in horizontal shale oil reservoirs, the effect of gravitational force is negligible.

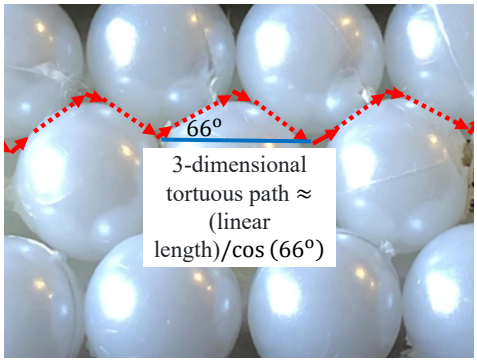

Fig. 3. Tortuous flow path between spherical grains.

The porous medium is assumed to be an ideal pack of spheric grains of uniform sizes as shown in Fig. 1. The angle between pore-channel axes is 114°. Fig. 2 illustrates a simplified model of pore space between solid grains of uniform sizes. Fundamental geometry gives an expression of the cross-sectional area (A_p) of the pore channel as:

$$A_p = \frac{D_g^2}{4}\left(\sqrt{3} - \frac{\pi}{2}\right) \tag{1}$$

where D_g is the equivalent diameter of the particle grain. The arc length (S_p) of each side wall of the pore is expressed as:

$$S_p = \frac{\pi}{6} D_g \tag{2}$$

The capillary pressure (p_c) is expressed as:

$$p_c = \frac{\sum_1^3 S_{pi}\sigma_i \cos\theta_i}{A_p} \tag{3}$$

where i is the index of pore sidewall, σ is interfacial tension (IFT), and θ is the contact angle measured in the wetting phase. The solid materials at the three walls can have different contact angles to the fluid in the pore. This allows for consideration of up to three types of minerals/organics surrounding the pore space. Fig. 3 depicts the tortuous flow path between spherical grain particles. It can be shown that the tortuous flow path is related to the linear length through $\cos 66°$, or 0.41, which is called tortuosity factor in this study.

The imbibition of wetting phase of fluid is promoted by the capillary force and resisted by viscous force. By applying Newton's second law of motion, the following imbibition model was derived in this study (see Appendix A for derivation):

$$x = \sqrt{\frac{\pi\left(2\sqrt{3} - \pi\right) D_g \sigma \sum_1^3 \cos\theta_i}{3\mu} t} \tag{4}$$

where x is the imbibition distance, μ is the viscosity of the wetting fluid, and t is imbibition time. It shows that fluid imbibition distance is proportional to the square root of time and inversely proportional to the square root of fluid viscosity. The effect of pore size on fluid imbibition is proportional to the equivalent diameter of grains that form the pore channel.

Eq. (4) reveals that CO_2 imbibition depth is proportional to the square root of CO_2 soaking time. The proportionality factor

is proportional to the square root of the product of pore size determined by grain size, CO_2 interfacial tension and variation of contact angle at the pore walls, and inversely proportional to the square root of CO_2 viscosity. Eq. (4) predicts CO_2 imbibition distance along a tortuous path. The true distance (depth) of imbibition in any direction should be counted after applying the tortuosity factor 0.41.

Eq. (4) is expected valid within the boundary of an area for free imbibition. For the area between two parallel fractures S_f apart, the boundary distance is $S_f/2$. Replacing x in Eq. (4) by $S_f/2$ and considering the tortuosity factor 0.41 gives the following equation for the maximal time of imbibition:

$$t_{\max} = \frac{3\mu S_f^2}{(2*0.41)^2 \pi \left(2\sqrt{3}-\pi\right) D_g \sigma \sum_1^3 \cos\theta_i} \tag{5}$$

$$t_{\max} = \frac{4.4\mu S_f^2}{D_g \sigma \sum_1^3 \cos\theta_i} \tag{6}$$

3. Model comparison

No clean data has been found to validate the model result yet, but a comparison of the expressions of capillary pressure used in this and in previous models can reveal some insight of the imbibition processes. Cai et al. (2014) presented a generalized mathematical model for spontaneous imbibition based on Hagen-Poiseuille flow in tortuous capillaries with variably shaped apertures. Their resultant model is as follows:

$$p_c = \frac{\sigma \cos\theta}{\alpha r_e} \tag{7}$$

where r_e is the equivalent capillary radius and α is a dimensionless geometry correction factor. They showed that α = 1 for a capillary with a circular cross section, α = 1.094 for a square, and α = 1.186 for an equilateral triangle.

Schwartz (1969) derived the following relation:

$$D_g = 6.5 d_p \tag{8}$$

where d_p is the dimeter of a circular capillary fitting to the pore space (shaded area in Fig. 2). Substituting this relation into Eq. (1) gives:

$$A_p = 6.28 r_p^2 \tag{9}$$

where $r_p = d_p/2$ is the radius of the circular capillary. Substituting Eq. (8) into Eq. (1) gives:

$$S_{p3} = 20.42 r_p \tag{10}$$

where $S_{p3} = 3S_p$ is the total length of the three concave arcs (perimeter of pore). The hydraulic diameter of the concave pore is expressed as:

$$d_h = \frac{4A_p}{S_{p3}} \tag{11}$$

Substituting Eqs. (9)-(10) into Eq. (11) gives:

$$d_h = 1.23 r_p \tag{12}$$

which yields an expression as a function of hydraulic radius r_p:

$$r_p = 0.81 r_h \tag{13}$$

Comparing Eq. (13) with Eq. (7) suggests that α = 0.81 for the 3-sided concave capillaries, i.e.,:

$$p_c = \frac{\sigma \cos\theta}{0.81 r_e} \tag{14}$$

This value of α being less unity suggests that the capillary pressure in concave capillaries is greater than that in circular capillaries. This makes sense because the perimeter on which the interfacial tension is acting in concave capillaries is greater than that in the circular capillaries. Nevertheless, this does not mean that the fluid imbibition is faster in concave capillaries than that in the circular capillaries because flow resistance due to fluid viscosity depends on the perimeter length.

4. Case study

A sensitivity analysis with the model was performed using the data from the Tuscaloosa Marine Shale (TMS). The TMS is part of the Tuscaloosa Group deposited along the northern Gulf of Mexico around 92 million years ago during the Cenomanian to Turonian stages of the late Upper Cretaceous (Lu et al., 2011). Core samples collected from well Sun #1 Spinks contain 40% to 65% rich clay (Lu et al., 2015). Borrok et al. (2019) found that most TMS core samples are characterized by a total clay content of 40 to 80 wt%, quartz of 20 to 40 wt%, and less than about 40 wt% calcite. The porosity measured was less than 4%, with permeability in the range of 10 to 79 nD. Yang and Handy (2020) estimated TMS permeability ranging from 53 to 210 nD using the production data of 16 TMS wells in Mississippi.

Valentine et al. (2016) analyzed the source rock potential of TMS based on core and cutting samples. Their results indicated that the Total Organics Content (TOC) of 99 samples ranged from 0.39 to 1.6 wt%, averaged 0.8 wt%. Based on the logging and laboratory petrophysical measurements of a TMS well, Besov et al. (2017) estimated the TOC of TMS in the range from 0.4 to 2.3 wt%, with an average of 1.6 wt%. Enomoto et al. (2017) studied the geological features of the TMS. Their interpretations indicated that the TMS contains dominantly Type III gas-prone kerogen and Type II oil-prone kerogen. The organic carbon content is between 0.14 and 4.0 wt%.

Experimental results of John et al. (1997) indicated that the porosity ranges from 2.3% to 8.0% and permeability ranges from less than 0.01 to 0.06 mD. Lohr and Hackley (2018) measured the porosity and absolute permeability of the Tuscaloosa Group in Mississippi using the mercury injection capillary pressure test method. Their result includes porosity ranging from 3.86% to 9.86%, with an average of 6.1%. The corresponding permeability was between 46 and 2,990 nD, averaged 427 nD.

Yang et al. (2024) analyzed production data from 79 wells completed between 2011 and 2016 in the emerging TMS play. One of their conclusions is that this TMS shares a 23% decline rate with Eagle Ford Shale (EFS) wells at the same age. The long-term performance of TMS wells, akin to EFS, not only validates the high quality of the core region but also unders-

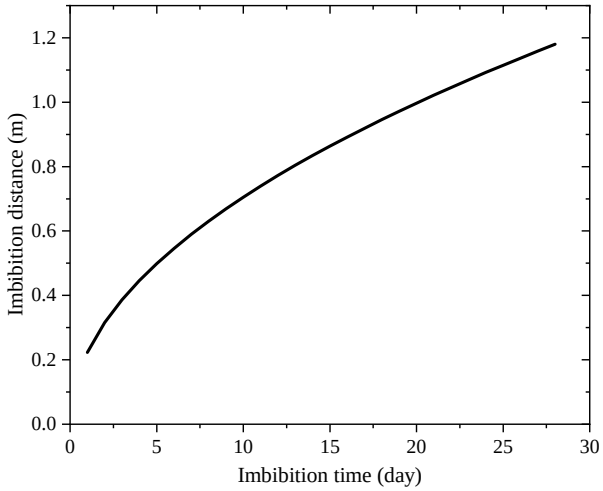

Fig. 4. Model-predicted CO_2 imbibition distance for the TMS formation.

Table 1. Pore and fluid properties in the TMS formation.

Parameter	Value	Unit
Grain diameter for pore size	0.00000159	m
CO_2 viscosity	0.000025	N-s/m^2
CO_2-methane IFT	0.000012	N/m
CO_2 contact angle to wall 1	15	degree
CO_2 contact angle to wall 2	40	degree
CO_2 contact angle to wall 3	60	degree

cores the overlooked yet promising production potential of this shale play. The great production potential comes from unoptimized hydraulic fracturing parameters including fracture spacing and the type and soaking time of fracturing fluid. The newly developed fluid imbibition is employed herein to identify the optimum post-frac soaking time of CO_2 as a hydraulic fracturing agent.

Berg (1970) presented the following correlation for estimating the permeability of particle packs:

$$k = 80.8\varphi^{5.1} D_{50}^2 e^{-1.385P} \tag{15}$$

where k is permeability in mD, D_{50} is the particle diameter in μm of 50 weight percentile and φ is porosity. The sorting term P (accounts for the spread in particle size) takes the form of:

$$P = 3.32 \log_{10} \frac{D_{10}}{D_{90}} \tag{16}$$

where D_{10} and D_{90} are the particle diameters in μm of 10 and 90 weight percentiles, respectively. For an ideal pack of spherical particles with D_{10}/D_{90} = 1, P = 0. Eq. (5) degenerates to:

$$k = 80.8\varphi^{5.1} D_{50}^2 \tag{17}$$

which allows for back estimating the equivalent particle diameter D_{50} if the porosity and permeability are known.

Based on the studies of Lohr and Hackley (2018), the porosity of TMS is in the range from 0.0386 to 0.0986, with an average of 0.061. Borrok et al. (2019)'s work gave a porosity less than 0.04, which is close to the lower bound of that of Lohr and Hackley (2018). Therefore, an average porosity 0.061 is used as a base line with the range used in sensitivity analysis that follows.

The permeability range measured by Lohr and Hackley (2018) is much higher than that estimated by Yang and Handy (2020) based on the production data analysis. This is because the former was measured in lab on dry cores. The permeability range given by Borrok et al. (2019) is close to the lower bound of that given by Yang and Handy (2020). Therefore, the later data set (0.000053 to 0.000210 mD with an average 0.000131 mD) is used in this study.

With a fixed value of porosity $\varphi = 0.061$, substituting k = 0.000053 mD, k = 0.000131 mD, and k = 0.000210 mD into Eq. (7) gives estimated maximum, average, and minimum particle sizes of 1.01, 1.59, and 2.02 μm.

The pressure in the TMS is typically considered "overpressured", meaning it is significantly higher than the hydrostatic pressure at that depth, with pressure readings varying depending on location, but generally ranging from several thousand psi to over 10,000 psi; the temperature in the TMS also varies based on depth, but is usually in the range of 200 °F to 300 °F. CO_2 viscosity at 8,000 psi and 250 °F is estimated to be 0.025 cp.

The IFT between liquid CO_2 and methane is typically low compared to other liquid-liquid systems, and significantly decreases with increasing pressure, generally ranging between 1-10 mN/m depending on the specific temperature and pressure conditions involved; essentially, as pressure increases, the distinction between the two phases becomes less defined, lowering the interfacial tension. The IFT is about 0.012 Dyne/cm at 8,000 psi and 250 °F (Amin et al., 2010).

The contact angle of liquid CO_2-methane on a rock surface is typically between 15° and 60°, indicating a moderately liquid-wet behavior, depending on the specific rock type, pressure, and temperature conditions; however, this can vary significantly depending on the rock's mineral composition and the exact mixture of CO_2 and methane present, with higher CO_2 concentrations potentially leading to a more CO_2-wet surface. The total organics content in shale can significantly increase the contact angle (Zhang et al., 2023).

Table 1 summarizes a generic dataset of the TMS for sensitivity analysis with the derived imbibition model. Sensitivity analysis was performed by changing one parameter at a time while keeping other parameter values unchanged.

Fig. 4 plots model-predicted CO_2 imbibition profile for the TMS formation with properties shown in Table 1. As implied by Eq. (4), the imbibition rate slows down with time due to the viscous force acting against the capillary force. It should take 1 week for the CO_2 to penetrate 0.6 m along the imbibition path, and it should take 4 weeks for the CO_2 to penetrate 1.2 m along the imbibition path.

Fig. 5 shows model-predicted effect of CO_2 contact angle on imbibition distance using the data in Table 1 except the contact nagle. The curves were generated for 4 scenarios: 1)

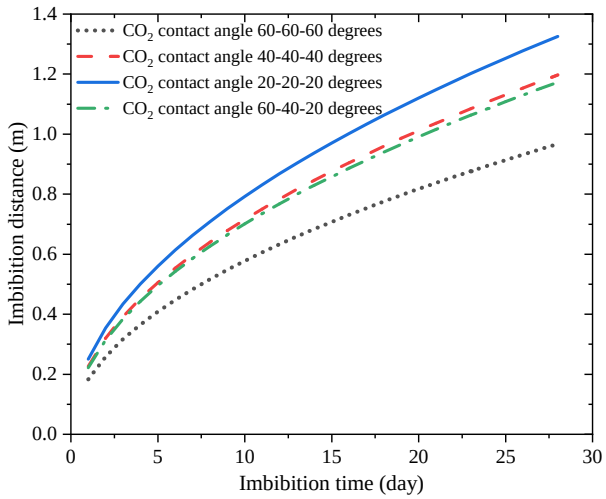

Fig. 5. Model-predicted effect of CO_2 contact angle on imbibition distance.

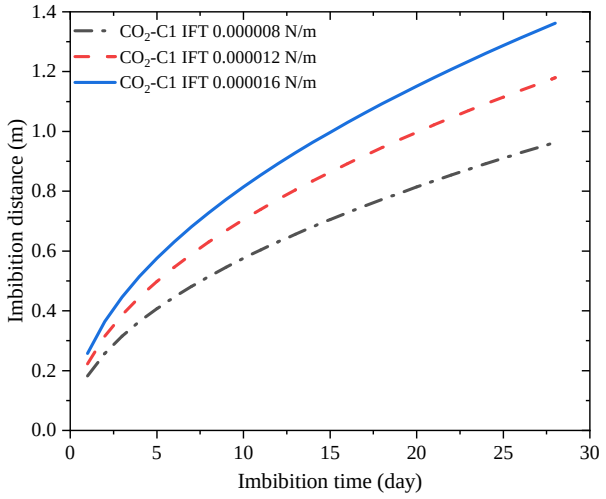

Fig. 7. Model-predicted effect of CO_2-methane interfacial tension on imbibition distance.

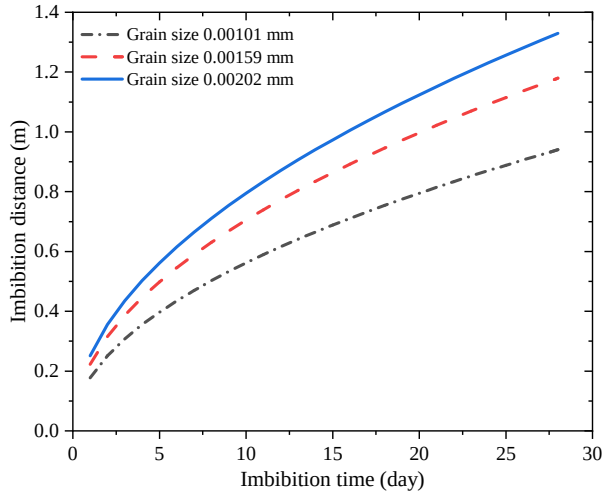

Fig. 6. Model-predicted effect of grain size on CO_2 imbibition distance.

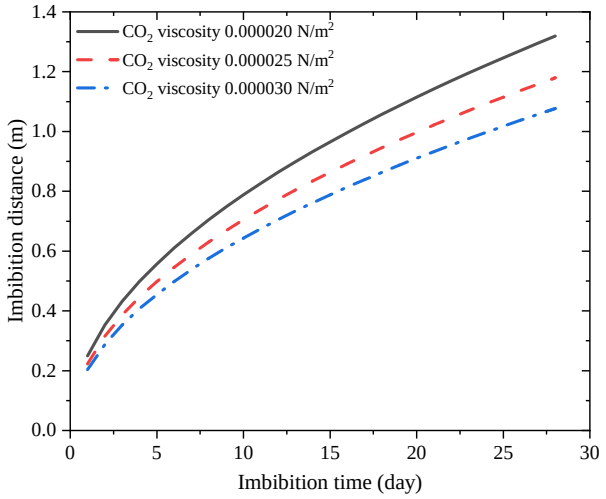

Fig. 8. Model-predicted effect of CO_2 viscosity on imbibition distance.

the same contact angle 60° at all three sides of the capillary, 2) the same contact angle 40° at all three sides of the capillary, 3) the same contact angle 20° at all three sides of the capillary, and 4) three contact angles 60°, 40°, and 20° at the three sides of the capillary. It demonstrates that the CO_2 penetration with the average contact angle 40° is greater than that with the three contact angles 60°, 40°, and 20° at the three sides of the capillary.

Fig. 6 demonstrates model-predicted CO_2 imbibition distances using the data in Table 1 except the grain size in a range from 0.00101 to 0.00202 mm. Small grain size corresponds to small pore size. The curves indicate that CO_2 imbibes slower in small size pores. This is due to the viscous resistance being larger in small pore channels than in large pore channels.

Fig. 7 shows model-predicted effect of CO_2-methane interfacial tension on imbibition distance using the data in Table 1 except the interfacial tension in a range from -50% to +50% around the average value of interfacial tension. The result suggests that CO_2-methane interfacial tension has a significant promoting effect on the CO_2 imbibition process. This is expected because interfacial tension is the driving force for spontaneous imbibition.

Fig. 8 presets a comparison of model-predicted CO_2 imbibition distances for 3 CO_2 viscosity values. It shows that the imbibition-distance is sensitive to CO_2 viscosity in the range of viscosity considered. Increases in CO_2-viscosity for any reason, such as foaming with water, should significantly reduce CO_2 imbibition. This is expected because fluid viscosity promotes resistant force for spontaneous imbibition.

5. Discussion

A quick comparison of the result from this case study with that presented by Mahmood et al. (2024) shows that the new model yields a faster imbibition than the circular capillary model. This is expected because Eq. (14) shows a greater capillary pressure by the concave triangle capillary model than the circular capillary model. Further investigations are needed to verify this observation.

It is understood that pressure and temperature have very significant effects on CO_2 properties, especial viscosity. Amar et al. (2020) presented two sets of correlations for predicting CO_2 viscosity. This subject is beyond the scope of this study and is not addressed in this paper.

Although the new imbibition model allows for simulating fluid imbibition in porous media with up to three major solid materials of different CO_2 wettability (contact angle), the effects of minor materials in the porous media may also be significant if their contact angles are low. It is recommended that the major solid materials be selected as the three materials with low-CO_2 contact angles.

People use complex computer models in simulation of fluid imbibition. Running these computer models is time-consuming and the accuracy of computer output is highly dependent on reliability of input data. The new analytical model is recommended to use in practical project for its simplicity, transparency, and high efficiency of computation with a trade-off of losing the effects of some minor factors such as multiphase flow.

6. Conclusions

A mathematical model was derived in this study to reveal the mechanism of CO_2 imbibition in shale formations considering the combined effects of capillary force and viscous force in concave curved triangle pore channels surrounded by different solid materials with different wettability (contact angles). Sensitivity studies with the model resulted in drawing the following conclusions.

1) CO_2 imbibition depth is proportional to the square root of CO_2 soaking time, square root of the pore size determined by grain size, square root of interfacial tension and cosine of contact angle, and inversely proportional to the square root of CO_2 viscosity.
2) The effect of organics content of shale formation on CO_2 imbibition can be analyzed using low CO_2 contact angles on the sidewalls of pore space in the model. Up to three materials with different contact angles can be considered in the model. Using the average contact angle for the three materials over-estimates the imbibition distance.
3) CO_2 imbibition is faster in concave curved triangle pores than in equivalent circular-shaped pores. The dimensionless geometry correction factor is less than unity (α = 0.81). This is because the perimeter, inducing imbibition due to interfacial tension, of the concave curved triangle pore is larger than that of the circular pore.
4) The newly developed imbibition model (Eq. (4)) is expected valid within certain time limit when the boundary of area for free imbibition is reached. For the area between two parallel fractures in multi–fractured shale formations, the maximum time of imbibition is given by Eq. (6).

Acknowledgements

The authors express their gratitude to the Northeast Petroleum University and the Energy Institute of Louisiana at the University of Louisiana at Lafayette for supporting the research.

Conflict of interest

The authors declare no competing interest.

References

Amar, M. N., Ghriga, M. A., Ouaer, H., et al. Modeling viscosity of CO_2 at high temperature and pressure conditions. Journal of Natural Gas Science and Engineering, 2020, 77: 103271.

Amin, R., Sidiq, H., Kennaird, T., et al. Gas–gas experimental interfacial tension measurement. Fluid Phase Equilibria, 2010, 295(2): 230-236.

Berg, R. R. Method for determining permeability from reservoir rock properties. Gulf Coast Association of Geological Societies Transactions, 1970, 20: 303-317.

Besov, A., Tinni, A., Sondergeld, C., et al. Application of laboratory and field NMR to characterize the Tuscaloosa marine shale. Petrophysics, 2017, 58(3): 221-231.

Borrok, D. M., Yang, W., Wei, M., et al. Heterogeneity of the mineralogy and organic content of the Tuscaloosa Marine Shale. Marine and Petroleum Geology, 2019, 109: 717-731.

Cai, J., Perfect, E., Cheng, C., et al. Generalized modeling of spontaneous imbibition based on Hagen-Poiseuille flow in tortuous capillaries with variably shaped apertures. Langmuir, 2014, 30(18): 5142-5151.

Cai, J., Sun, S., Wang, H. Current advances in capillarity: Theories and applications. Capillarity, 2023, 7(2): 25-31.

Cai, J., Yu, B. A discussion of the effect of tortuosity on the capillary imbibition in porous media. Transport in porous media, 2011, 89(2): 251-263.

Enomoto, C. B., Hackley, P. C., Valentine, B. J., et al. Geologic characterization of the hydrocarbon resource potential of the Upper Cretaceous Tuscaloosa marine shale in Mississippi and Louisiana, USA. Gulf Coast Association of Geological Societies Transactions, 2017, 67(1): 95-110.

Fakher, S., Fakher, A. Investigating the use of CO_2 as a hydraulic fracturing fluid for water sustainability and environmental friendliness. Paper Presented at SPE/IATMI Asia Pacific Oil & Gas Conference and Exhibition, 12-14 October, 2021.

Gupta, N., Verma, A. Supercritical carbon dioxide utilization for hydraulic fracturing of shale reservoir, and geostorage: A review. Energy & Fuels, 2023, 37(19): 14604-14621.

John, C. J., Jones, B. L., Moncrief, J. E., et al. An unproven unconventional seven billion barrel oil resource-The Tuscaloosa Marine Shale. BRI Bulletin, 1997, 7: 1-22.

Lohr, C. D., Hackley, P. C. Using mercury injection pressure analyses to estimate sealing capacity of the Tuscaloosa

marine shale in Mississippi, USA: Implications for carbon dioxide sequestration. International Journal of Greenhouse Gas Control, 2018, 78: 375-387.

Lu, J., Milliken, K., Reed, R. M., et al. Diagenesis and sealing capacity of the middle Tuscaloosa mudstone at the Cranfield carbon dioxide injection site, Mississippi, USA. Environmental Geosciences, 2011, 18(1): 35-53.

Lu, J., Ruppel, S. C., Rowe, H. D. Organic matter pores and oil generation in the Tuscaloosa marine shale. AAPG bulletin, 2015, 99(2): 333-357.

Mahmood, M. N., Nguyen, V., Guo, B. Challenges in mathematical modeling of dynamic mass transfer controlled by capillary and viscous forces in spontaneous fluid imbibition processes. Capillarity, 2024, 11(2): 53-62.

Middleton, R., Viswanathan, H., Currier, R., et al. CO_2 as a fracturing fluid: Potential for commercial-scale shale gas production and CO_2 sequestration. Energy Procedia, 2014, 63: 7780-7784.

Schwartz, D. H. Successful sand control design for high rate oil and water wells. Journal of Petroleum Technology, 1969, 21(9): 1193-1198.

Sinal, M. L., Lancaster, G. Liquid CO_2 fracturing: Advantages and limitations. Journal of Canadian Petroleum Technology, 1987, 26(5).

Song, X., Guo, Y., Zhang, J., et al. Fracturing with carbon dioxide: From microscopic mechanism to reservoir application. Joule, 2019, 3(8): 1913-1926.

Valentine, B. J., Hackley, P., Enomoto, C. B., et al. Preliminary evaluation of source rock potential and burial history of the Upper Cretaceous Tuscaloosa marine shale in Mississippi and Louisiana, USA. Paper Presented at AAPG Annual Convention and Exhibition, Calgary, Alberta, Canada, 19-22 June, 2016.

Yang, B., Wang, H., Li, G., et al. Fundamental study and utilization on supercritical CO_2 fracturing developing unconventional resources: Current status, challenge and future perspectives. Petroleum Science, 2022, 19(6): 2757-2780.

Yang, X., Guo, B. Statistical analyses of reservoir and fracturing parameters for a multifractured shale oil reservoir in Mississippi. Energy Science & Engineering, 2020, 8(3): 616-626.

Yang, X., Ruse, C. M., Wortman, P. B., et al. Clay-rich Tuscaloosa marine shale: Production decline analysis. Paper Presented at Unconventional Resources Technology Conference, Texas, USA, 17-19 June, 2024.

Zhang, J., Zhao, Z., Xu, Z., et al. Surface wettability of sandstone and shale: Implication for CO_2 storage. International Journal of Greenhouse Gas Control, 2023, 126: 103917.

Zou, Y., Li, N., Ma, X., et al. Experimental study on the growth behavior of supercritical CO_2-induced fractures in a layered tight sandstone formation. Journal of Natural Gas Science and Engineering, 2018, 49: 145-156.

Appendix A. Derivation of analytical model of fluid imbibition in nanopores between particle grains with different wetting properties

Mass transfer in nanoscale pore channels is driven by capillary force, resisted by viscous friction force, and promoted or demoted by gravitational force, depending on orientation of the flow relative to gravity. For the fluid imbibition in shale oil reservoirs, horizontal seepage is essential. Therefore, the effect of gravitational force is negligible.

Appendix A.1 Governing equation

The capillary force acting on the fluid over an area of porous channel can be formulated based on interfacial tension, contact angle, and perimeter of capillary channel. It is customary to express the capillary force as a function of capillary pressure:

$$F_c = A_p p_c \tag{A1}$$

where F_c is capillary force in N, A_p the cross-sectional area of the capillary channel in m^2, and p_c is capillary pressure in N/m^2. For a capillary channel with a concave curved triangle cross-section shown in Fig. 1, the capillary pressure is expressed as:

$$p_c = \frac{\sum_1^3 S_{pi}\sigma_i \cos\theta_i}{A_p} \tag{A2}$$

where i is the index of side i of the channel wall, S_p is the wall length of the pore in m, σ is interfacial tension in N/m, and θ is the contact angle measured in the wetting phase. Based on the contact points of the spheric grains, the length of each side wall is expressed as:

$$S_p = \frac{\pi}{6} D_g \tag{A3}$$

where D_g is the equivalent diameter of the particle grain in m. The cross-sectional area of the pore throat is expressed as:

$$A_p = \frac{D_g^2}{4}\left(\sqrt{3} - \frac{\pi}{2}\right) \tag{A4}$$

Substituting Eqs. A3-A4 into Eq. A2 yields:

$$p_c = \frac{2\pi\sigma\sum_1^3 \cos\theta_i}{3\left(\sqrt{3} - \frac{\pi}{2}\right) D_g} \tag{A5}$$

Substituting Eqs. A4-A5 into Eq. A1 gives:

$$F_c = \frac{\pi D_g \sigma \sum_1^3 \cos\theta_i}{6} \tag{A6}$$

The viscous friction force F_f acting on the fluid over an imbibition depth x is expressed as:

$$F_f = A_p P_f \tag{A7}$$

where F_f is friction force in N, P_f is friction pressure in N/m^2. Assuming laminar flow, Poiseuille's law applies. It gives:

$$P_f = \frac{8\mu x}{\pi r_h^4} Q \tag{A8}$$

where μ is the wetting fluid viscosity in $N\text{-}s/m^2$, x is penetration of imbibition in m, and r_h is hydraulic radius in m, and Q is flow rate in m^3/s. The flow rate Q is approximated by:

$$Q = A_p \frac{\mathrm{dx}}{\mathrm{dt}} \tag{A9}$$

where t is time in second. Submitting Eq. A9 into A8 yields:

$$P_f = \frac{8\mu A_p}{\pi r_h^4} x \frac{\mathrm{dx}}{\mathrm{dt}} \tag{A10}$$

Substituting Eq. A10 into Eq. A7 gives:

$$F_f = \frac{8\mu A_p^2}{\pi r_h^4} x \frac{\mathrm{dx}}{\mathrm{dt}} \tag{A11}$$

For horizontal imbibition processes where gravity effect is zero, applying Newton's second law of motion to the flowing fluid gives:

$$F_c - F_f = \rho A_p x \frac{\mathrm{d}^2\mathrm{x}}{\mathrm{dt}^2} \tag{A12}$$

where ρ is fluid density in kg/m^3. Substitutions of Eqs. A6 and A11 into Eq. A12 yield:

$$\frac{\pi D_g \sigma \sum_1^3 \cos\theta_i}{6} - \frac{8\mu A_p^2}{\pi r_h^4} x \frac{\mathrm{dx}}{\mathrm{dt}} = \rho A_p x \frac{\mathrm{d}^2\mathrm{x}}{\mathrm{dt}^2} \tag{A13}$$

which is simplified to yield:

$$-A\frac{\mathrm{dx}}{\mathrm{dt}} - \frac{B}{x} = \frac{\mathrm{d}^2\mathrm{x}}{dt^2} \tag{A14}$$

where

$$A = \frac{8\mu A_p}{\pi r_h^4 \rho} \tag{A15}$$

$$B = -\frac{\pi D_g \sigma \sum_1^3 \cos\theta_i}{6\rho A_p} \tag{A16}$$

Appendix A.2 Initial conditions

The governing equation Eq. A14 can be solved using the following initial conditions:

$$x = x_0, \text{ at } t = 0 \tag{A17}$$

$$\frac{\mathrm{dx}}{\mathrm{dt}} = v_0, \text{ at } t = 0 \tag{A18}$$

Appendix A.3 Solution

The solution of Eq. A14 was given by Mahmood et al. (2024). It does not converge at t = 0 due to singularity. In the region away from the singularity, the acceleration $\mathrm{d}^2\mathrm{x}/\mathrm{dt}^2$ is negligible. Then Eq. A14 becomes:

$$\frac{\mathrm{dx}}{\mathrm{dt}} + \frac{B}{Ax} = 0 \tag{A19}$$

which takes an integration form of:

$$\int_0^x x\mathrm{dx} = -\frac{B}{A}\int_0^t \mathrm{dt} \tag{A20}$$

which is integrated to yield:

$$x = \sqrt{-\frac{2B}{A}t} \tag{A21}$$

Substituting Eqs. A15-A16 into Eq. A21 results in a solution for imbibition in porous media:

$$x = \sqrt{\frac{\pi^2 D_g \sigma r_h^4 \sum_1^3 \cos\theta_i}{24\mu A_p^2}t} \tag{A22}$$

The hydraulic radius, based on definition, is expressed as:

$$r_h = \frac{2A_p}{\sum_1^3 S_{pi}} = \frac{2A_p}{3S_p} \tag{A23}$$

Substituting Eqs. A3-A4 into Eq. A23 gives:

$$r_h = \frac{D_g\left(\sqrt{3} - \frac{\pi}{2}\right)}{\pi} \tag{A24}$$

Substituting Eqs. A4 and A24 into Eq. A22 results in a solution for imbibition in porous media:

$$x = \sqrt{\frac{\pi\left(2\sqrt{3} - \pi\right) D_g \sigma \sum_1^3 \cos\theta_i}{3\mu}t} \tag{A25}$$